Engineering Geology 354 (2025) 108152

Contents lists available at ScienceDirect

Engineering Geology

journal homepage: www.elsevier.com/locate/enggeo

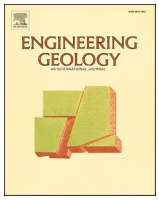

Scale-dependent recursive analysis of topographical roughness: A methodology for differentiating geological and geomechanical features from point cloud data

Niloufarsadat Sadeghi *, Jonathan D. Aubertin

École de Technologie Supérieure, ÉTS, 1100 Notre-Dame St W, Montréal, Québec H3C 1K3, Canada

ARTICLE INFO

Keywords:
Remote Sensing
Rock Engineering
Fractals
Geomorphology
Geomechanical Differentiation
Roughness
Topographical Features
LiDAR

ABSTRACT

Exposed rock surfaces reflect diverse topographical features shaped by underlying geological and geomechanical conditions, such as mineral composition, weathering, excavation methods, and structural geology. These features directly influence the mechanical behavior of in-place materials, providing a robust basis for differentiating geological and geomechanical units in engineering. Their explicit spatial differentiation relies on time-consuming and subjective visual assessments, or the inefficient and difficult to reproduce measurement of topographical features (e.g., roughness, undulation) at arbitrary scales. This work aims to offer an objective, reproducible, and efficient topographical analysis framework to differentiate geological and geomechanical features arising from natural and man-made origins. This study introduces a scale-dependent recursive analysis method to systematically evaluate and characterize roughness conditions of exposed rock surfaces. By analyzing point clouds across multiple scales, the method derives scale-dependent trends and computes parameters that distinguish topographical features associated with specific geological and operational settings. A moving-window algorithm is applied as a second layer of analysis to capture localized trends, integrating these as an explicit scalar field within point clouds for direct differentiation of features. This methodology improves accuracy and efficiency compared to traditional roughness measurement techniques by reducing biases and subjectivity associated with visual-based assessments. The approach is demonstrated using four datasets from diverse geological and geomechanical contexts, showcasing its applicability and the insights gained. The influence of point cloud density and moving-window size on the recursive analysis is further discussed, highlighting the method's potential to provide objective and quantifiable topographical differentiation for mining, tunneling, and construction applications.

1. Introduction

Exposed rock surfaces exhibit widely variable topographical features reflecting upon the broad geological and geomechanical conditions observable. The topographical nature of an exposed outcrop depends on a plurality of factors, such as mineral composition, weathering and alteration, excavation method, structural geology, etc. Conversely, features which affect topographical conditions of rock surfaces directly influence the mechanical behavior of the in-situ material, and thus provide robust grounds for objective differentiation of geological and geomechanical units in engineering applications.

Figure 1 exemplifies the broad extent of plausible topographical conditions along natural and excavated rock outcrops. Such conditions directly influence conventional interpretation towards engineering classifications and design practices. Fig. 1 (a) shows a picture of the infamous Vajont (Italy) rockslide event (Hoek, 2007) for a historical perspective on the event and its influence on modern rock engineering. The exposed rock surface is characterized by a smooth and persistent discontinuity plane. Such topographical conditions highlight the post-failure nature of the sheared asperities along the sliding plane. Fig. 1 (b) shows an excavated bench at a limestone quarry. The open face orientation bends from near parallel strike with respect to camera orientation on the left, to near perpendicular on the right. The change in open face orientation leads to very different topographical conditions dictated by the natural joint incidence angle. The left section of the figure exhibits pronounced stepping of the blocks along the open face.

* Corresponding author.
E-mail address: niloufarsadat.sadeghi.1@ens.etsmtl.ca (N. Sadeghi).

https://doi.org/10.1016/j.enggeo.2025.108152
Received 13 January 2025; Received in revised form 15 April 2025; Accepted 22 May 2025
Available online 23 May 2025

The right section presents a flatter surface due to near parallel face strike with one of the discontinuity sets. Fig. 1 (c) presents a limestone quarry near Montreal, Canada. The exposed rock face exhibits volcanic intrusions through the sedimentary layers in the form of a near-vertical dyke on the left, and a horizontal sill near the bottom of the bench. The different geological units along the face present different levels of fracture intensity and weathering, which are easily recognized by the different topographical conditions observed. Fig. 1 (d) presents a freshly blasted roadcut featuring prevalent blasthole traces from engineered perimeter blasting practices. The resulting face is characterized by a smooth and consistent plane formed by the radial fractures connecting the blastholes.

The examples illustrated in Fig. 1 underscore the inherent correlation between topographical features and geomechanical conditions. It is thus asserted that topographical characterization can provide a robust and systematic framework towards geological and geomechanical differentiation in the context of engineering applications.

Traditional methods for characterizing rock surfaces primarily rely on visual assessments and subjective interpretations, often leading to inconsistencies in classification and limiting reproducibility. While such assessments provide a practical and intuitive understanding of rock mass behavior, they typically evaluate rock surfaces based on qualitative descriptors, lacking standardized and quantifiable parameters that ensure consistency and comparability across different studies or practitioners. Furthermore, these methods often simplify complex surface variations by grouping multiple geological or geomechanical sub-units into broad classification categories. Such oversimplifications fail to capture the inherent heterogeneity of rock masses, where distinct mechanical properties may exist within seemingly homogeneous units. Consequently, these limitations can lead to inaccurate assessments, misinterpretations of discontinuity behavior, and suboptimal engineering designs.

Table 1
Parameters and acronyms of reference for this work.

Parameter/ Acronym	Description
TLS	Terrestrial laser scanner
RMSD	Root Mean Square Deviation
ξ_r (m)	Overall roughness of a surface with respect to the scale of measurement r
A, H	Scale dependent regression parameters for $\xi_r - r$
D	Fractal dimension
RMS	Root Mean Square
N	Number of points within a circle of radius r
LiDAR	Light Detection and ranging
H	Hurst exponent
r (m)	Radius of roughness measurement
$R_{r,i}$	Roughness value for the point P_i measured at r (m)
$\bar{s}$	Average point spacing
r_w	Radius of local spheres centered around point P_i

The present work introduces an analytical, computational, and procedural framework for topographical differentiation of exposed rock interfaces in geoengineering applications. Unlike conventional approaches that rely heavily on visual assessments, this framework integrates advanced computational techniques to establish a reproducible and quantifiable method for characterizing rock surfaces. A key contribution of this study is the development of a multi-scale, data-driven approach that systematically captures topographical patterns of various geological units along rock surfaces, representing them with unique quantitative descriptors at local scales. This approach leverages high-

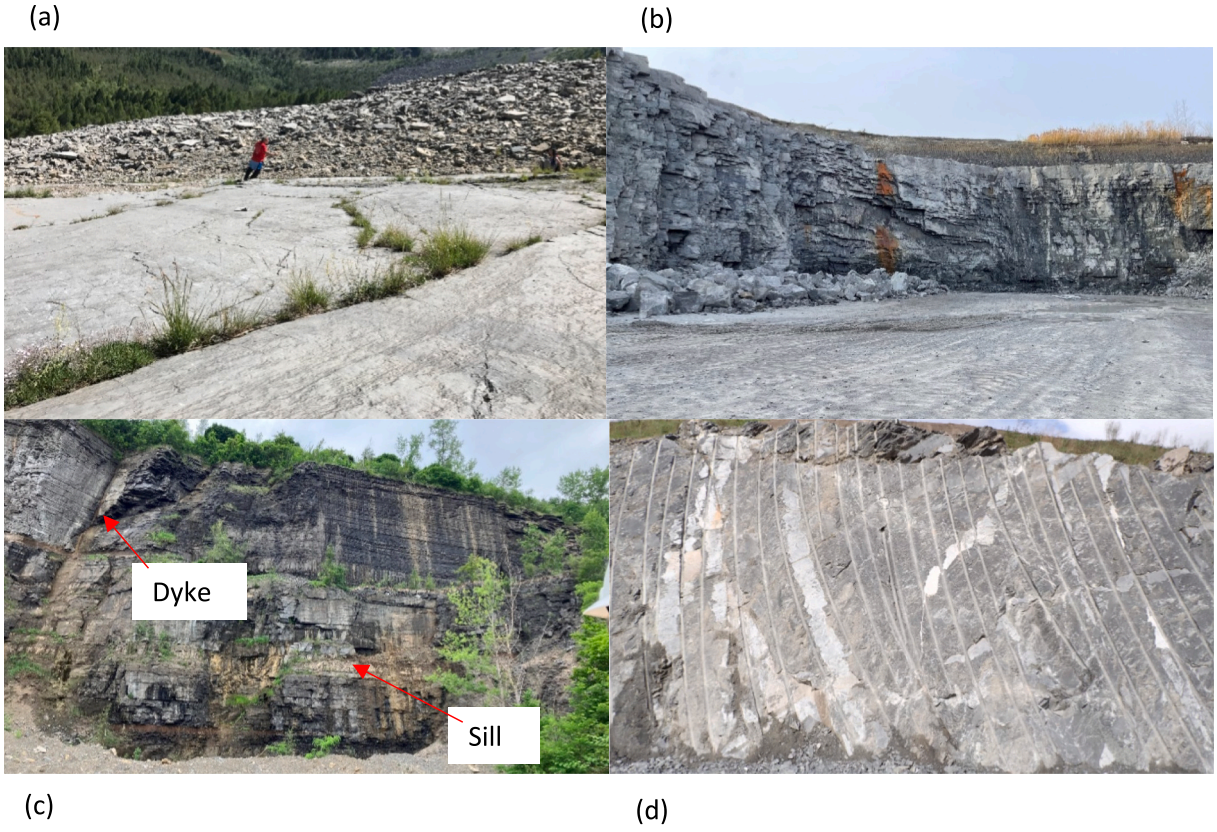

Fig. 1. (a) the Vajont (Italy) rock slide discontinuity plane characterized by smooth interface caused by intense shearing following the instability event; (b) limestone quarry with face orientation varying from near perpendicular strike on the left to near parallel strike on the right with respect to camera point of view; (c) aggregate quarry in a sedimentary deposit with distinct vertical (dyke) and horizontal (sill) volcanic intrusions; (d) road cut with visible blastholes following perimeter blasting to achieve a smooth resulting surface.

resolution point cloud data, automated roughness extraction, and clustering algorithms to enhance the objectivity and accuracy of rock mass assessments. This study provides a structured methodology that enables precise differentiation of geological and geomechanical units based on measurable criteria. Systematic topographical characterization explicitly contributes to efficient geomechanical differentiation, offering practical benefits in mining, tunneling, and construction applications. Furthermore, the proposed methodology facilitates a standardized and objective comparison of exposed outcrops under varying geological conditions, improving predictive modeling, stability analysis, and engineering design decisions.

The present research implements a Scale-dependent recursive analysis method to evaluate roughness conditions and differentiate topographical features associated with specific geological and geomechanical conditions. Roughness is measured at different scales from surveyed point clouds to derive scale-dependent trends. The computed parameters provide the basis to formulate topographical characteristics for various geomechanical features and operational settings (e.g., excavation method). A moving-window based algorithm is then applied to evaluate the local scale-dependent trends. This second layer of recursive analysis is integrated as an explicit scalar field into the point cloud to offer a direct differentiation scheme for topographical features. Cumulative passing distribution analysis is also conducted to support spatial and operational clustering. The approach is exemplified through four datasets surveyed from different geological and geomechanical settings to showcase the application framework and derived results. The selection of these case studies aimed to capture a broad spectrum of geomechanical and operational conditions reflected directly by topographical features. A discussion is later provided on the influence of point cloud density and the size of the moving windows for the second layer of recursive analysis. The effectiveness of the proposed method is evaluated through case studies selected from known geological settings, where contrasting features were pre-identified. These case studies serve as a form of back analysis, allowing for the comparison of the methodology's performance against expected geological and geomechanical outcomes. While the features were known beforehand, the evaluation focuses on how well the method differentiates and quantifies these features, providing a robust framework for assessing its applicability in real-world scenarios. Symbols and acronyms for this work are outlined in Table 1.

2. Background

Topographical conditions along rock outcrops are often represented by the broadly defined concept of roughness. According to the International Society of Rock Mechanics (ISRM, 1978), surface roughness represents the extent of asperities and undulations relative to the fitted flat plane at the considered scales. Roughness plays a central role in numerous empirical classifications (Barton et al., 1974; Bieniawski, 1989; Hoek and Marinos, 2007), and shear strength criteria (Grasselli, 2001; Liu et al., 2017; Singh and Basu, 2018; Barton et al., 2023).

Various formulations have been proposed to capture linear (*2D*) and planar (*3D*) discontinuity geometries and roughness characteristics (Tatone and Grasselli, 2010; Azarafza et al., 2019; Magsipoc et al., 2020; Azarafza et al., 2021; Guo et al., 2022; Liu et al., 2022). Barton (1973) introduced the term "Joint Roughness Coefficient" (*JRC*) which is an empirical measure employed to assess the impact of roughness on the shear strength of rock interfaces. *JRC* has since been converted into quantifiable measurements and reproducible topographies for systematic evaluation (Zheng and Qi, 2016; Liu et al., 2017; Stigsson and Mas Ivars, 2019; Bao et al., 2020). Nevertheless, scale limitations and the subjective nature associated with *JRC* and similar empirical measurements led to mathematical and statistical representations of roughness for objective comparison purposes. These computational frameworks leverage topographical surveys from remote sensing tools (e.g., *LiDAR*, photogrammetry) to derive quantifiable measurements.

Magsipoc et al. (2020) presented a detailed review of various computational and statistical frameworks to evaluate *2D* and *3D* roughness for geoengineering applications. In this review, Magsipoc and collaborators describe at length fractal-based (i.e., scale-dependent) computational methods given their potential for objective differentiation and scalability of the measurements. The applicability of such fractal models has also been investigated in a number of other studies (Lee et al., 1990; Hyslip and Vallejo, 1997; Bagde et al., 2002; Fardin et al., 2004; Kolay and Kayabali, 2006; Fardin, 2008; Tatone and Grasselli, 2013; Lai et al., 2014; Li and Huang, 2015; Li et al., 2023).

Expanding from procedural algorithms presented by Shepard et al. (2001), Aubertin and Hutchinson (2022) implemented a fractal-like scale-dependent approach to compare various rock surfaces characterized by different excavation methods or conditions (e.g., blast damage intensity and corresponding ground control efforts). A power formulation was proposed to correlate overall roughness ξ_r (m) of a surface with respect to the scale of measurement r (m).

$$\xi_r = Ar^H \tag{1}$$

where A and H are parameters that characterize topographical trends occurring over a range of different scales. The exponent H in Eq. [1] is often referred to as the Hurst exponent which can be correlated to different geometrical features. The fractal dimension D (m) describes the scaling properties of an irregular geometry, and is measured from H using the relation $D = 3 - H$ for a *3D* profile (Mandelbrot, 1967).

Various statistical approaches to describe the overall roughness of surfaces exist (Tatone and Grasselli, 2010; Berti et al., 2013; Lê et al., 2018). These representations are determined through the use of averaging techniques such as the arithmetic mean and the root mean square (*RMS*) (Shepard et al., 2001; Chae et al., 2004; Ban et al., 2020; Ge et al., 2022). Other statistical representations of roughness may involve assessing the spatial variation between points to measure the topographical gradient and determine the angle of inclination (e.g., Glenn et al., 2006; Lai et al., 2014; McKean and Roering, 2004; Poropat, 2008; Tatone and Grasselli, 2013).

In this study, the overall roughness of a given topographical dataset (ξ_r) (m) is assessed using Root Mean Square Deviation (*RMSD*) of measured point roughness values at given scales of r ($R_{r,i}$):

$$\xi_r = \sqrt{\frac{1}{N-1}\sum_{1}^{N}\left(R_{r,i} - \overline{R}_r\right)^2} \tag{2}$$

where N is number of points, and $\overline{R}_r$ (m) is the measured point roughness average at for radius of measurement r.

Figure 2(a) plots overall roughness ξ_r for the topographical model of a rock face shown in Fig. 2(b) surveyed in an underground mine (adapted from Aubertin and Hutchinson (2022)). The plot presents overall roughness with respect to scale r in a log-log plane. The data points follow consistent power trends following the formulation of Eq. [1] over two distinct ranges of radii of measurement r. The different ranges where Eq. [1] is consistently observed differentiate the distinct topographical features at small scales (e.g., fractures, joints, asperities) versus large scales (e.g., face undulation, blastholes toe).

Aubertin and Hutchinson's (2022) work underscored the potential to leverage the parameters of Eq. [1] to compare different mining conditions such as the performance of blasting methods, ground control settings, mining dilution, and mechanical scaling efforts (see also Aubertin et al., 2019). Sadeghi et al. (2023) further explored the potential of scale-dependent roughness measurements to contrast geological and geomechanical features. Until now, these studies required manual segmentation of the different sections to explicitly compare their respective topographical conditions. The present work automates this process through a two-layer recursive algorithm to provide a systematic differentiation framework.

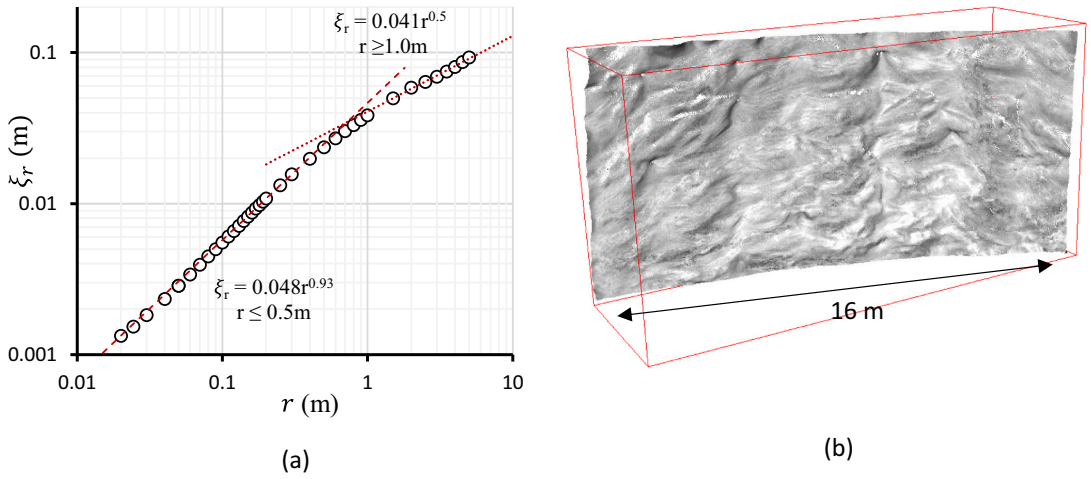

Fig. 2. (a) Overall roughness with respect to scale for the rock face illustrated in (b). Datasets originally presented in (Aubertin and Hutchinson, 2022).

3. Experimental methods

3.1. Scale-dependent roughness analysis

The proposed recursive algorithm is based on the three-dimensional definition of roughness. In this work, roughness refers to the local deviation from planarity. Roughness values of *3D* point cloud models are measured as the shortest distance between individual points and best-fit local planes. Considering a point $P_i = [x_i, y_i, z_i]$, the *3D* roughness $R_{r,i}$ (m) of that point is computed as the distance between the plane best fitted by all points within a radius r (m) from point P_i. That plane is described by its normal vector $\overrightarrow{n_{r,i}} = [a_{r,i}, b_{r,i}, c_{r,i}]$. Roughness $R_{r,i}$ (i.e., the distance between the plane and point P_i) is computed by the following equation:

$$R_{r,i} = \frac{a_{r,i}x_i + b_{r,i}y_i + c_{r,i}z_i}{\sqrt{a_{r,i}^2 + b_{r,i}^2 + c_{r,i}^2}} \tag{3}$$

Roughness measured using Eq. [3] is by definition scale dependent. Aubertin and Hutchinson (2022) underscored that different scales of measurements reflect different features along natural and excavated rock outcrops. For example, a large radius of measurement (> 1 m) will typically reflects upon the overall topography of the rock face, highlighting changes in face orientation, undulation, and excavation related damage if any. By contrast, roughness measurement at small scale (≤ 0.5 m) will highlight superficial fractures, fissures, and the crystalline matrix of the rock mass.

Figure 3 highlights the influence of scale in roughness measurements. The figure shows a freshly blasted face at an underground mine. Roughness was measured with radii of measurement r of 0.1 and 2 (m) respectively. Roughness measurement at small scale reflect very localized asperities and protrusions, while the larger scale of measurement emphasizes lumps and blasthole remnants.

Roughness values and their resulting statistical representations like ξ_r (Eq. 2) are highly dependent upon the scale of measurement r. In this study, scale-dependent behavior of topographical datasets is evaluated by plotting ξ_r against the radius of measurement in log-log plane (Fig. 2). Linear trends (in the log-log plane) can be extracted to fit the relationship of Eq. [1], and derive characteristic parameters A, H and fractal dimension D. It will next be demonstrated that the variability of these trends can be leveraged to differentiate geological and geomechanical conditions.

3.2. Automated moving window analysis

Exposed rock outcrops often present variable topographical features which differentiate operational and geomechanical conditions. The spatial distinction between different topographical units is achieved by applying the concept of scale-dependent trend measurements recursively. The procedural framework is outlined next, and was

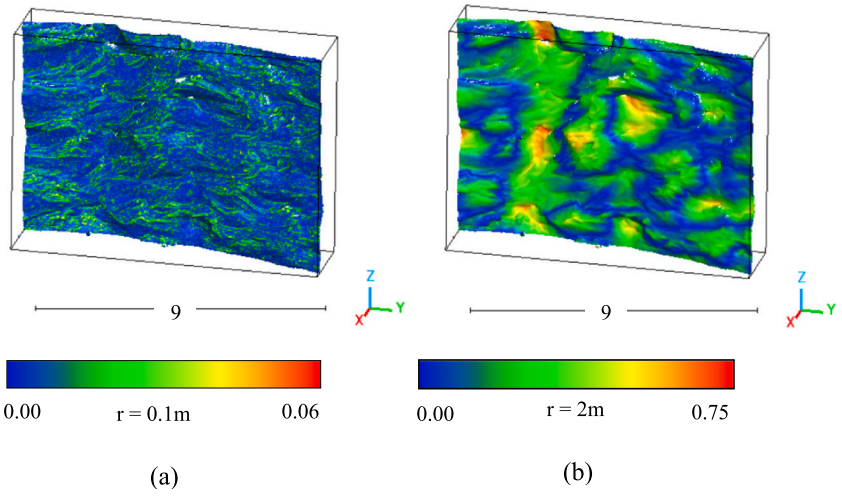

Fig. 3. Point roughness visualization at (a): small scale and (b): large scale.

implemented in Python version 3.11.7 (Python Language Reference, 2023).

Roughness values for different radii of measurement ($R_{r,i}$) are computed for all data points of the topographical dataset (Eq. [3]). Overall roughness ξ_r (Eq. [2]) is computed for a subset of the cloud defined by a sphere of radius r_W (m) centered around point P_i. Overall roughness ξ_r is computed for each point of the dataset and for each radius r considered.

A linear regression is performed between log (ξ_r) and log(r) to obtain parameters A and H (Eq. [1]) for each point. As noted in Fig. 2 (a), different sets of parameters A and H may be computed from the analysis. In this work, A and H are computed exclusively from $r < 1$ m. This imposed restriction ensures that the analysis focuses on topographical conditions at the rock block scale rather than at full excavation scale. The implications of this assumption are discussed further in a later section.

The procedural workflow described above is summarized by a series of steps representing a readily scripted algorithm. For each point P in cloud C:

1: Compute the normal vector $\vec{n}$ corresponding to a best-fit plane[1] for all points within a distance r from point P.
2: Compute the roughness $R_{r,i}$ of point P, i.e., the distance between the point and the best fit plane defined at step 1 (Eq. [3]).
3: Repeat steps 1 and 2 for all radii of measurement r required.
4: Compute the *RMSD* (ξ_r, Eq. [2]) with respect to all $R_{r,i}$ measured for all points within a distance r_w from point P, for all radii of measurement r required.
5: Evaluate the linear regression between log(ξ_r) and log(r) to determine coefficient A, exponent H, and parameter $D = 3 - H$.

The above procedural workflow requires a defined range of radii r to perform the linear regression trend, and compute scale-dependent parameters A, H and D. Aubertin and Hutchinson (2022) noted that different trends can be observed at different ranges of radii. A change in trend signifies a change in dominating features, e.g., crystal size morphology at small scale and excavation profile at larger scale. In this work, a preliminary assessment of scale-dependent trends is performed on large sections of the dataset to evaluate the testing range $r_{min} \leq r \leq r_{max}$. r_w is determined based on the multiple factors, including scan density (for all case studies, local scale-dependent trends were observed for $r \geq 10\times$ average point spacing, $\bar{s}$), the intended application and the extent of the scan.

4. Experimental applications

4.1. Differentiating exposed rock from massive support in advancing tunnel

The first case study was selected from a point cloud model of an advancing underground tunnel, surveyed using a FARO X-130 (FARO Technologies, 2021) terrestrial laser scanner (TLS). The studied span includes two distinctly different surfaces: a shotcrete-covered section and the exposed rock surface of the tunnel wall. This initial example serves as a proof of concept, highlighting the noticeable contrast between these two surfaces. A span of approximately 5.5 m × 6 m was selected from the surveyed area, with an average point spacing of 0.01 m. Fig. 4 shows a dataset representing the tunnel's topographical model.

Scale-dependent topographical trends were first computed for the entire dataset to evaluate characteristic scale thresholds. Fig. 5 (a) plots overall roughness ξ_r with respect to radius of measurement r for the full dataset. Two linear trends are observed at $0.03 \leq r \leq 0.5$ and $r \geq 0.5$ and it is also inferred that the topographical behavior of the cloud below $r < 0.03$ m reflects upon point density. The cloud was then manually segmented to explicitly distinguish the two surface types. Fig. 5 (b) plots overall roughness ξ_r with respect to radii of measurement r for the two distinct subsets. The most consistent and distinguishable trends are observed for the different subsets in the range of $0.05 \leq r \leq 0.5$. Above this range, it is inferred that topographical conditions are dominated by tunnel geometry.

Based on the observations from manual measurements, recursive topographical classification was conducted at $0.05 \leq r \leq 0.5$, following the workflow outlined in the previous section. After testing a range of r_w values, the smallest value at which meaningful local trends were observed was 0.1 m, which is 10 times the average point spacing of the cloud. To better assess the algorithm's performance and compare classification quality, another r_w value, almost twice the smallest possible one was also tested. Fig. 6 and Fig. 7 show results of the analysis, with point cloud color scale for the parameters A, D and D/A.

The plots in Figs. 6 and 7 highlight the topographical divergence between the two different surfaces considered. The recursive algorithm assigns scale-dependent values associated with trends regressed from roughness measurements. The plots offer similar level of resolution for both spherical radii r_w, and it is thus inferred that the selection of that parameter is more subject to the intended application rather than topographical nature of the surfaces, as long as it exceeds a certain limit, which in this case study is approximately 10 times the average point spacing of the point cloud. However, smaller r_w values result in greater data loss compared to larger ones, as a smaller radius reduces the likelihood that a local neighborhood contains enough points to meet the algorithm's conditions for the minimum number of points required to measure *RMSD* of point roughness values. As a result, these neighborhoods are excluded from the cloud.

It is asserted from the spatial distribution of scale-dependent parameters observed in Figs. 6 and 7 that a threshold value can be determined to differentiate objectively topographical zones. Fig. 8 plots the model with binary color scale threshold of $D/A = 150$ for $r_w = 0.1$ m and 0.25 m. The concrete-lined section is clearly differentiated in the model. It is noted that although the distribution for r_w=0.25 is better than that for r_w=0.1, it is not yet perfect. However, it reflects a distinctive statistical distribution associated with the scale-dependent parameter. This later notion offers additional benefits towards quantifying spatial variability as discussed in a later section.

4.2. Structural differentiation along open pit slope

The topographical differentiation algorithm was applied along a slope section of an active open-pit mine. The pit walls were surveyed using a FARO X-130 TLS with 1/8 resolution (12 mm point spacing per 10 m increments) and repeated point measurements of three times. The selected span presents a discernible wedge failure creating two intersecting surfaces with respect to the blasted pit profile. The analysis carried out in this example aimed to differentiate the different sliding surfaces and contrast roughness conditions from the design pit wall.

Fig. 9 shows the topographical model investigated as part of this case study. The extent of the segmented part is about 7.5 m × 10.5 m with an average point spacing of approximately 0.02 m. The pit wall shown in Fig. 9 strikes due South. The two sub-vertical structures delineating the failure event are henceforth referenced as the North (left in the figure) and South (right in the figure) faces.

Preliminary scale-dependent roughness analysis was carried on the topographical dataset shown in Fig. 9. Fig. 10 (a) plots the overall roughness ξ_r with respect to scale of measurement r for the dataset. Trends for the $\xi_r - r$ relationships consistent with Eq. [1] formulation are noted in the figure. Transition scales are observed at $r = 0.2$ m and $r = 1$ m. The scale-dependent parameters change for $r > 1$, reflecting a change in scale of dominant features. The trend below $r < 0.1$ also diverges, reflecting upon point spacing of the point cloud.

[1] See algorithm presented in Stewart (2003) or Aubertin and Hutchinson (2022)

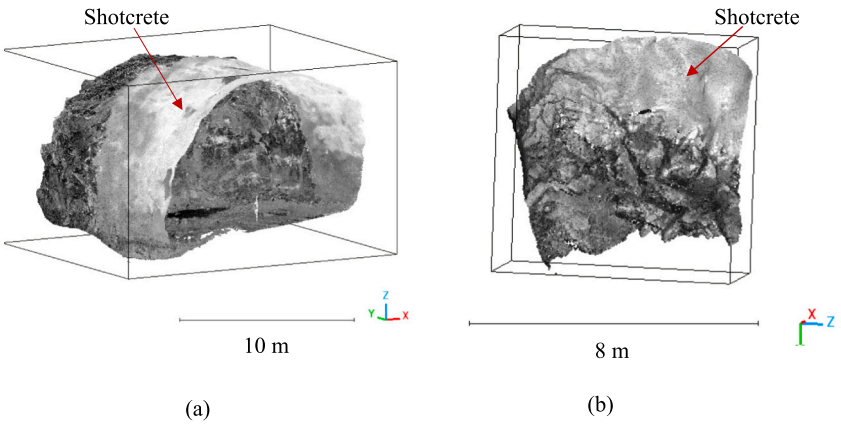

Fig. 4. 3D point cloud model of (a) the whole span of the advancing tunnel dataset from a pseudo-isometric view and (b) plan view of the subset analysed.

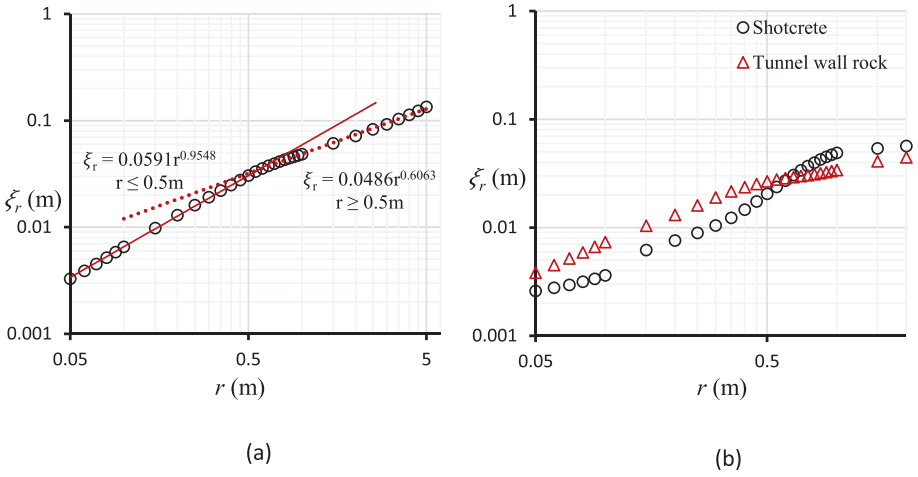

Fig. 5. ξ_r with respect to radius of measurement r (in log-log planes) for (a) the entire studied span from the advancing tunnel dataset and (b) segmented sections of contrasting surfaces (shotcrete and tunnel wall rock).

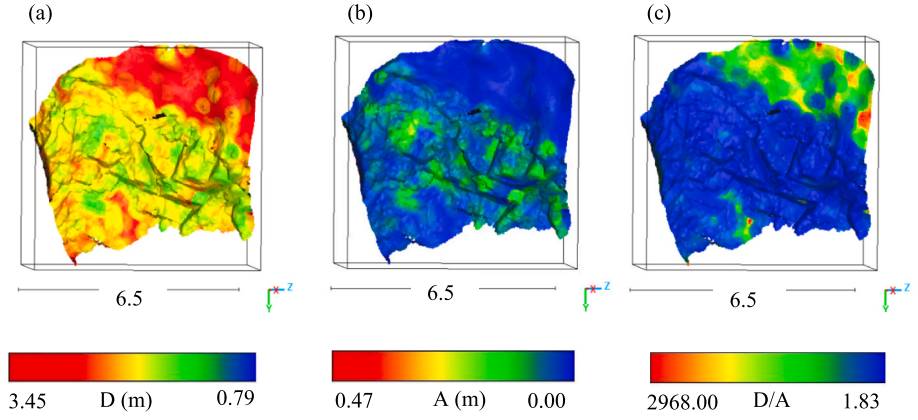

Fig. 6. Visualization of local scale-dependent parameters (a) D, (b) A, and (c) D/A using scalar fields on the advancing tunnel dataset, with spherical neighborhood radius of 0.25 m.

Scale-dependent roughness analysis was also carried out on manually segmented sections of the dataset corresponding to the two structural planes seen in Fig. 9, and a section of the pit wall. Fig. 10 (b) plots the $\xi_r - r$ relationships for the three sections. Various trends are denoted from the different curves with different transition scales. It is asserted that the transition scales highlighted with Fig. 10 (a) are valid for all three different morphologies, and these are therefore implemented in the automated recursive analysis.

Automated recursive scale-dependent analysis was performed on the topographical dataset with a radius range of $0.1 < r < 1$ m. Similar to the previous example, different r_w values were tested for the differentiation algorithm. The smallest value where a meaningful trend could be observed was 0.1, which is approximately 10 times the average point spacing of the cloud. Another r_w value, nearly twice the smallest one,

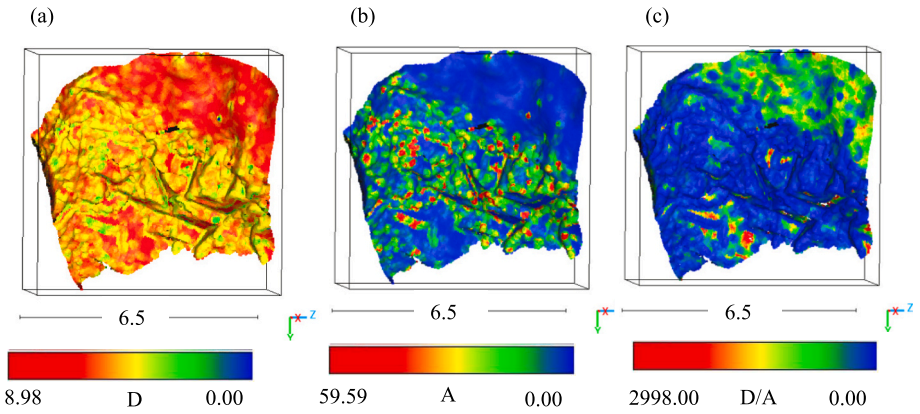

Fig. 7. Visualization of local scale-dependent parameters (a) D, (b) A, and (c) D/A using scalar fields on the advancing tunnel dataset, with spherical neighborhood radius of 0.1 m.

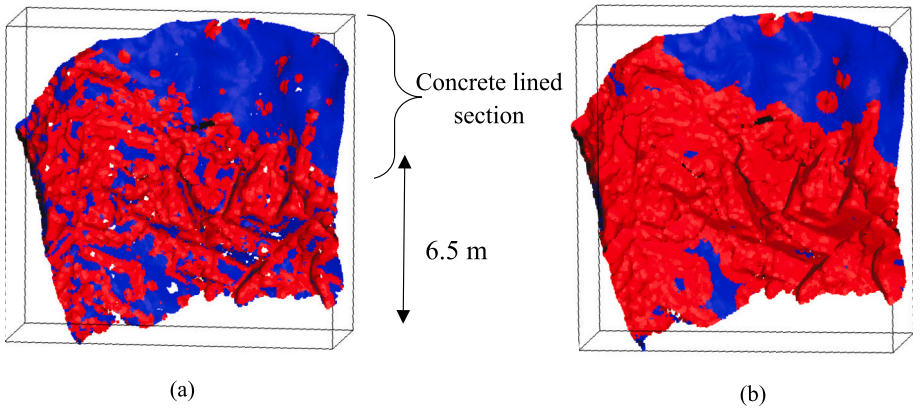

Fig. 8. Topographical model of the tunnel subsection with binary color scale for D/A with threshold value of 150 for (a) $r_w = 0.1\ m$ and (b) $r_w = 0.25\ m$.

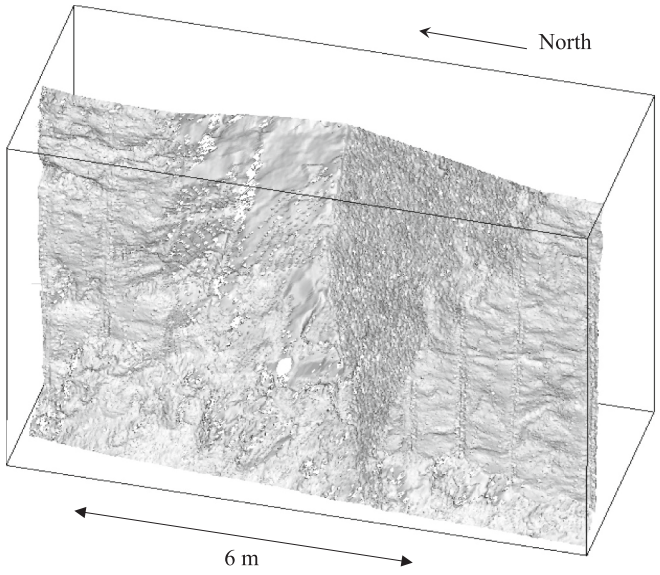

Fig. 9. 3D point cloud model of the surveyed area from the graphite mine consisting of a wedge failure.

was also tested to compare the classification quality. Figs. 11 and 12 show the topographical dataset with color scales for parameters D, A, and D/A with moving spherical window of radius $r_w = 0.25$ and 0.1 m, respectively.

The classification results in Figs. 11 and 12 are quite similar for both spherical radii r_w. However, $r_w = 0.1$ captures finer local variations, while $r_w = 0.25$ provides a more continuous distribution. Since this case study aims to differentiate broader-scale structural trends, $r_w = 0.25$ offers a clearer representation. The plots for parameter D for both r_w values provide stark contrast between the structural surfaces and the pit wall with notable statistical variability. By contrast, the plots for parameter A present consistent scalar distribution along the distinct surfaces. The plots for D/A present discernible profiles that can be subdivided into three distinct profiles: structural (sheared) surfaces, pit wall, and damaged rock mass at the bottom of the wedge. It can be noted for all three plots that the North structural plane shows consistent trends along its central portion, while the edges show roughness conditions comparable to the broken rock mass section at the bottom of the wedge extent. It is inferred that the instability event involved sliding (and intense shearing) along the South plane (right on the figure) and a portion of the North plane, compounded with tensile breakage along the edges. Shearing of asperities is made apparent by a steep $\xi_r - r$ relationship in the log-log plane (i.e., high parameter D) which implies low roughness conditions at small scale.

4.3. Topographical variability with the mining cycle of an advancing tunnel

The next case study investigates scale-dependent topographical features measured along blasted rock surfaces in an underground mine. The original dataset was presented in Aubertin and Hutchinson (2022). Rock blasting is followed by mechanical scaling of tunnel walls as part of the standard mining cycle. Fig. 13 shows the topographical datasets and

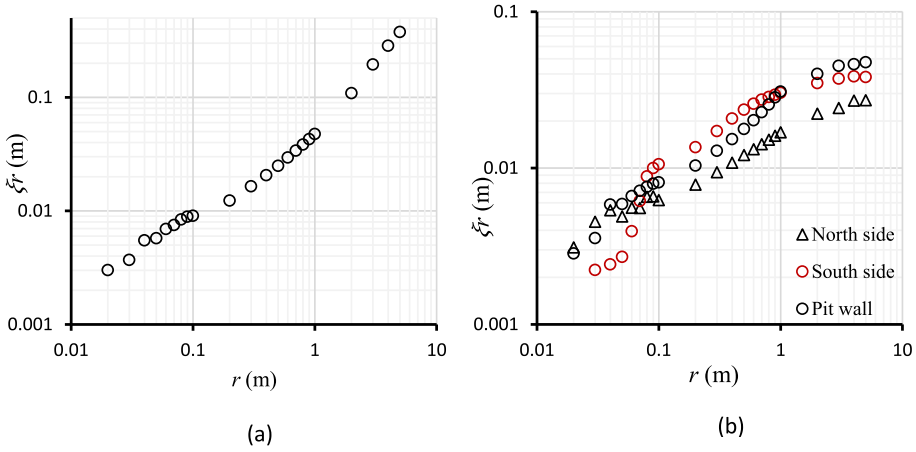

Fig. 10. ξ_r with respect to scale for (a) the entire studied span from the graphite mine dataset and (b) segmented sections of contrasting surfaces.

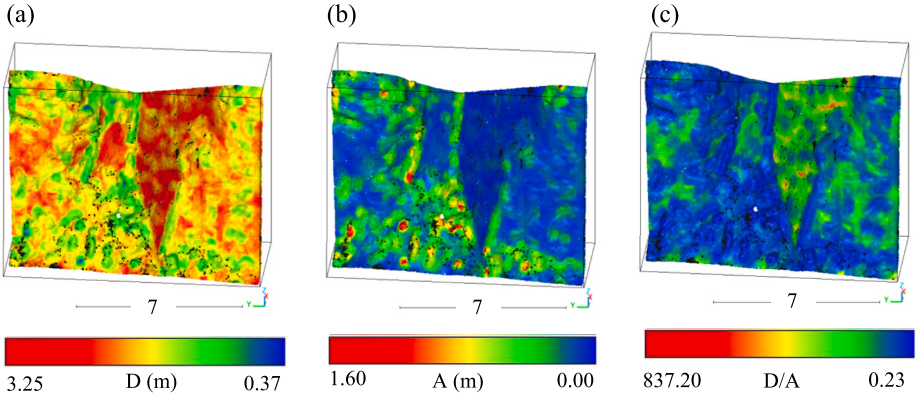

Fig. 11. Visualization of local scale-dependent parameters using scalar fields on the graphite mine dataset, with spherical neighborhood radius of 0.25 m.

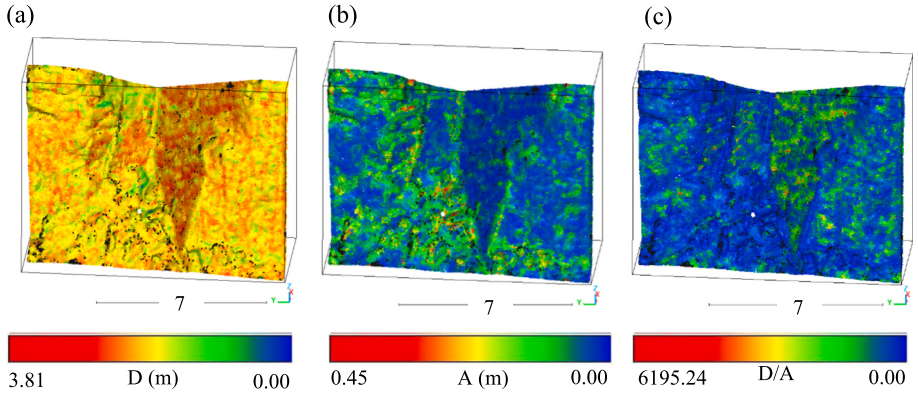

Fig. 12. Visualization of local scale-dependent parameters using scalar fields on the graphite mine dataset, with spherical neighborhood radius of 0.1 m.

the roof subset considered for the investigation. The studied span covers approximately 4.8 m × 9 m with an average point spacing of 0.01 m.

The dataset contrasts the freshly blasted section of the roof from normal post-scaling conditions. Overall roughness ξ_r was measured and plotted on a log-log scale in Fig. 14 (a). Fig. 14 (b) plots ξ_r with respect to scale of measurement for manually segmented subsets of the model to contrast observed conditions. It is noted from the preliminary manual investigation shown in Fig. 14 (b) that topographical trends differ within the range of radii of measurement of $0.1 \leq r \leq 1$ m, with the blasted surfaces exhibiting higher roughness values. Topographical behavior of the cloud below and above this range is mostly dominated by the cloud density and tunnel geometry, respectively.

The automated recursive scale-dependent analysis was applied to the roof section of the model shown in Fig. 13 for $0.1 \leq r \leq 1$. Considering the cloud's average point spacing and the objective of this case study, differentiating topographical patterns across different mining cycles, a spherical measurement radius of $r_w = 0.25$ m was selected. This choice ensures the capture of larger-scale topographical trends associated with different mining cycles.

Figure 15 shows the model with color scale for parameters D, A, and D/A. It is noted from the figure that parameter D, associated with exponent H, presents significant spatial variability without meaningful

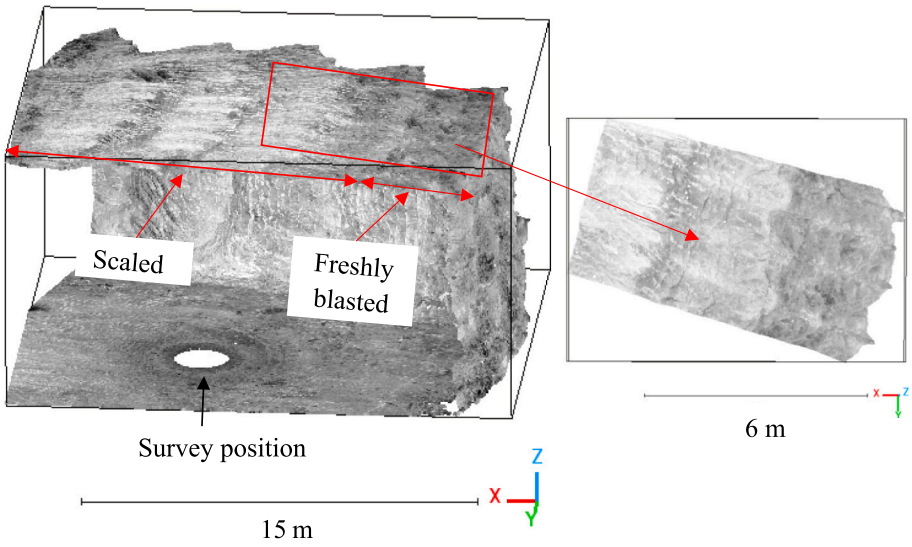

Fig. 13. 3D point cloud model of surveyed area consisting of freshly-blasted and scaled sections along the mine drift.

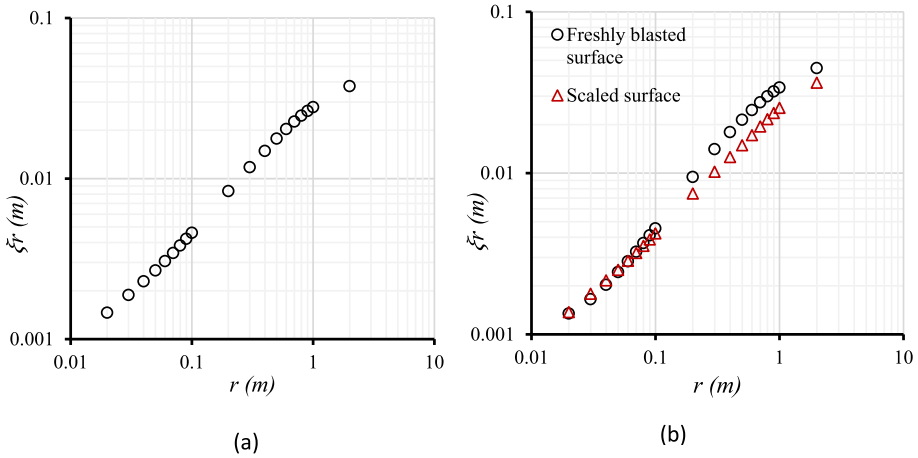

Fig. 14. ξ_r with respect to scale for (a) the entire studied span from the Pugwash mine drift dataset and (b) segmented sections of contrasting surfaces.

differentiable sections. In contrast, parameter A displays apparent zoning. These latter observations concur with trends observed in Fig. 14, as the slope of the trends in the log-log plane were seemingly parallel (parameter D), and presented a curve offset (parameter A) along the considered range of radii.

Further investigation of the distribution for D/A seemingly shows a progressive increase in parameter D/A from left to right in Fig. 15, corresponding to a decrease in overall roughness from the blasted front to the scaled section. Fig. 16 plots the model with binary color scale, and with a threshold of $D/A = 110$. The figure also distinguishes the three consecutive advance rounds associated with the mining cycle. It is inferred from the plot that the freshly blasted section presents the largest spatial concentration of high roughness conditions. The second round of the mining advance received one scaling cycle, and therefore presents a lower proportion of high roughness conditions. The last segment on the left of the figure corresponds to a section scaled on multiple occasions, and presents much lower overall roughness than the other two sections.

4.4. Weathering and mechanical erosion contrasts

The next case study is part of an ongoing research program to evaluate the impact of cyclical snow and winter debris dumping along rock slopes at an abandoned limestone quarry (Niknezhad et al., 2024). The surfaces impacted by material dumping are characterized by severely accentuated weathering conditions induced by poor drainage, freeze-thaw cycles and mechanical erosion. The blocky structures of the quarry are defined by 2 sub-vertical joint sets and a recurring horizontal sedimentary lithology mostly composed of limestone with occasional shale horizons. The severe weathering results in the near-complete superficial erosion of the blocky structures, creates a new artificial structural plane striking perpendicular to the dumping direction, and results in substantial weakening of the localized rock mass. The algorithm introduced in this research was applied to a section of the pit wall to differentiate spatially the geomechanical conditions observed.

Figure 17 shows an isometric view of the quarry. Remnants of winter and snow debris are present at the bottom of the pit. This accumulation tends to remain present almost year-round, which notably impact the drainage conditions along the slope. A large concrete pad is used for truck dumping of the snow debris, which impact the rock slope of the abandoned quarry.

The pit walls were surveyed using a drone-mounted DJI Zenmuse L1 LiDAR coupled with a D-RTK station. The resulting topographical dataset has a point spacing of 6 cm. Fig. 18 shows an isometric view of the topographical dataset collected from the LiDAR survey. The detailed analysis was conducted for the upper half of the dataset corresponding to the first 10 m high bench of the abandoned quarry (this zone is identified as the extended zone of investigation on the figure).

Preliminary scale-dependent analysis was carried out on the full

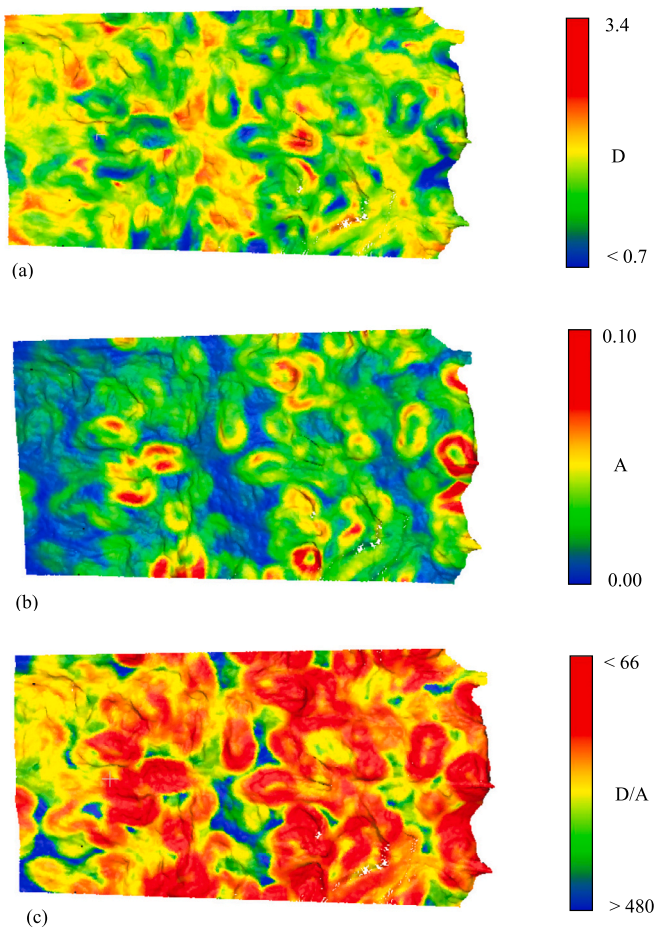

Fig. 15. Topographical model of the tunnel roof section with color scale for parameters (a) D, (b) A, and (c) D/A.

dataset and two manually selected subsets (identified in Fig. 18) of the cloud to determine the scale of interest for topographical differentiation purposes. Fig. 19 shows the overall roughness ξ_r with respect to radius of measurement r for the two subsets corresponding to blocky structures and pronounced weathering and mechanical erosion. The presence of linear trends with varying slopes and intercepts across different scales of measurement represents the dominance of distinct features at each scale.

From Fig. 19, it is noted that the trends for $r < 1$ m are comparable between the two contrasted surfaces. It is inferred that the associated small-scale topographical features pertain to the local geological units consistent for the two zones. The trends seemingly diverge after $r > 1$ m for the weathered surface. It is thus inferred that the induced mechanical weathering is observable at a much larger scale than in the previous case studies, and corresponds to larger geomorphological features. From this preliminary analysis, the investigation range is set to 1 m $\leq r \leq$ 7 m.

The recursive scale-dependent topographical analysis was performed on the upper bench identified in Fig. 18. The analysis was conducted for the range of 1 m $\leq r \leq$ 7 m, with moving-window spherical radius of $r_w = 5m$. Similar to previous case studies, selection of r_w is based on the average point spacing of the scan and the intended application which is determined from the defined range for the algorithm where the scale-dependent topographical trends of the studied geomorphological features remain distinguishable. Fig. 20 plots the distribution of the scale-dependent parameter values computed for the topographical dataset. In the figure, the distribution values (horizontal axis) are normalized by the mean of the measured parameter. All distribution curves represent the same cumulative total number of data points. It can be observed from the distribution of measured parameter D (associated with exponent H) presents two relative peak values. These distinct peaks are also clearly discernible in the D/A distribution. It is inferred that these two subsets of the distributions correspond to the different topographical (i.e., geomechanical) conditions of interest noted for this case study. As noted with Fig. 19, the differentiated trends for the different topographical units are characterized by distinct slopes (i.e., exponent H and parameter D) in their respective $\log(\xi_r)$ - $\log(r)$ trends.

Fig. 21 shows the topographical dataset investigated with three different color scales for parameters D, A, and D/A. The plots for

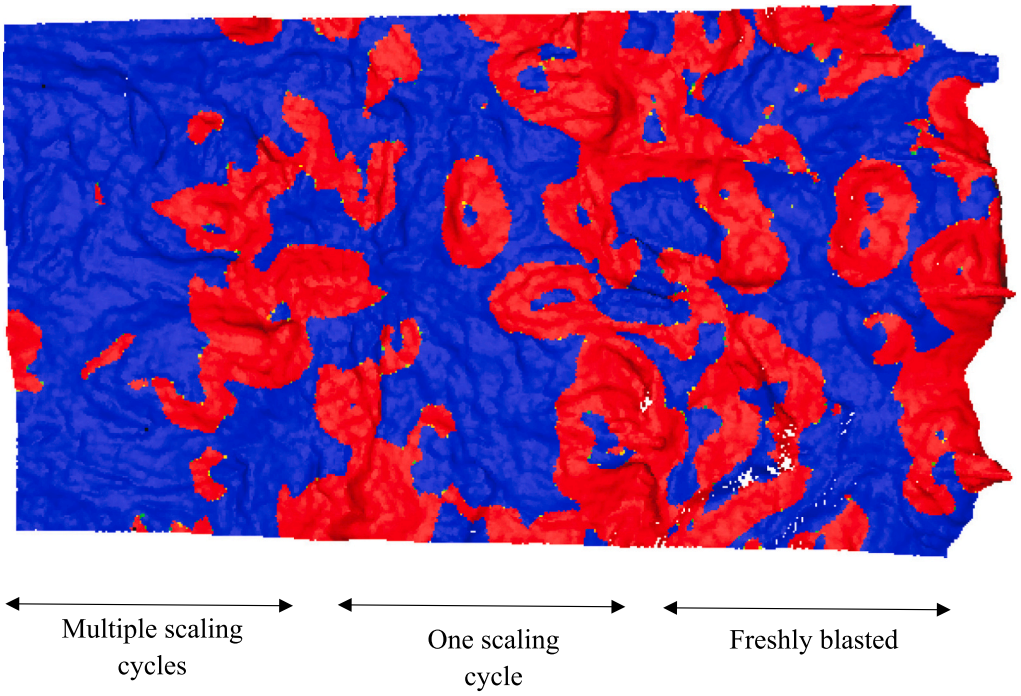

Fig. 16. Topographical model of the mine tunnel roof section with binary color scale using a threshold of $D/A = 110$.

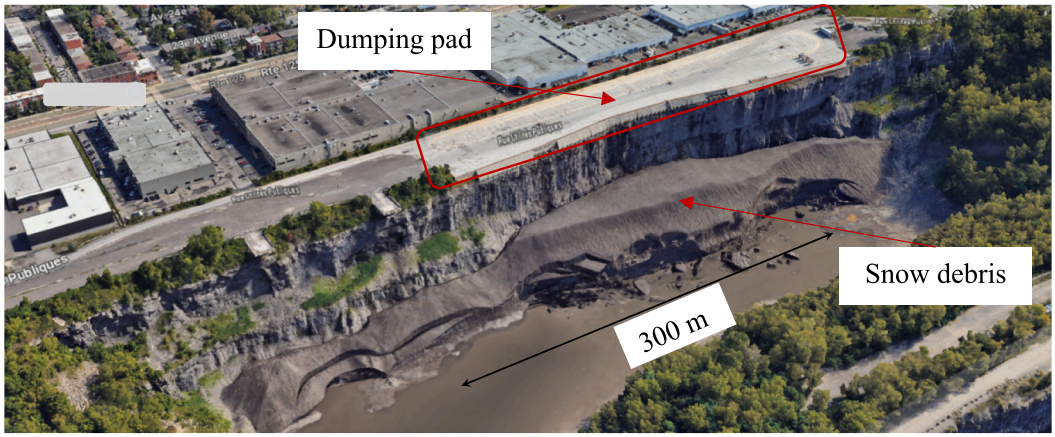

Fig. 17. Isometric view of an abandoned limestone quarry located in Montreal, Canada. The pit is used for winter and snow debris storage dumped from a large concrete pad. Severe weathering and mechanical erosion arise from the intensive cyclical and seasonal dumping.

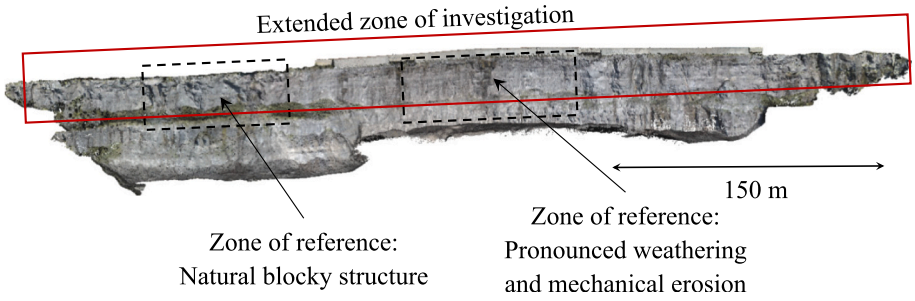

Fig. 18. Topographical dataset of the limestone quarry used for winter debris storage.

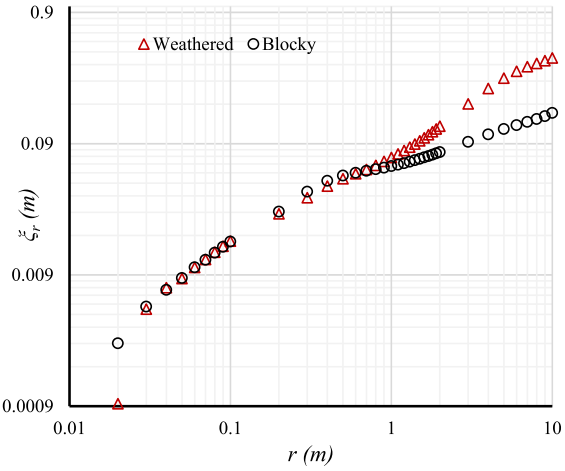

Fig. 19. ξ_r with respect to scale for (a) full dataset and (b) the zones of reference corresponding to natural blocky structure along the pit wall and pronounced weathering and mechanical erosion near the dumping points.

parameter D and D/A show a distinct variation in topographical parameters within the horizontal position range of 145 m to 362.5 m. This range is consistent with the denoted zone of dumping observed in Fig. 18. The values measured for the different parameters present statistical variability as expected given the geomorphological conditions. It is inferred however that distinct threshold values can be leveraged to differentiate topographical conditions. This approach is investigated in the next section for the different case studies presented in this research.

The threshold approach is again leveraged to distinguish the different topographical zones. Fig. 22 shows the topographical model with binary color scale and D/A threshold value of 34. The weathered zone is clearly delineated between 145 m and 362.5 m. Spatial variability is still present in this example, and it is inferred that local anomalies reflect distinct topographical features. For example, the zone near 290 m appears to have sustained a structural instability which would explain the localized topographical conditions. It is thus inferred that a predetermined number of differentiated subzones may not always be achievable, and this topographical investigation provides a more objective framework towards classification of subsets.

5. Discussion

The research presented in this work highlighted the strong correlation between topographical features and geomechanical conditions. The approach presented an objective method to differentiate different clusters through a specific set of geometric criteria. The results showed important spatial and statistical variability with respect to topographical measurements. Such variability is to be expected in most geoengineering applications, and it is often in fact part of the design process to determine a confidence threshold and an associated analytical framework towards distinct geomechanical classifications.

Spatial variability was observed with all four case studies investigated. The concrete-lined tunnel section presented the most apparent topographical contrast between the two types of interfaces. It is noted from Fig. 8 that binary differentiation is near perfect, albeit some small overlap in topographical criteria along the two surfaces. The advancing mine tunnel and the pit wall case studies revealed pronounced spatial variability. Further investigation revealed that the preliminary clustering criteria may have been insufficient. The advancing tunnel revealed three distinct zones with variable roughness intensity. In this

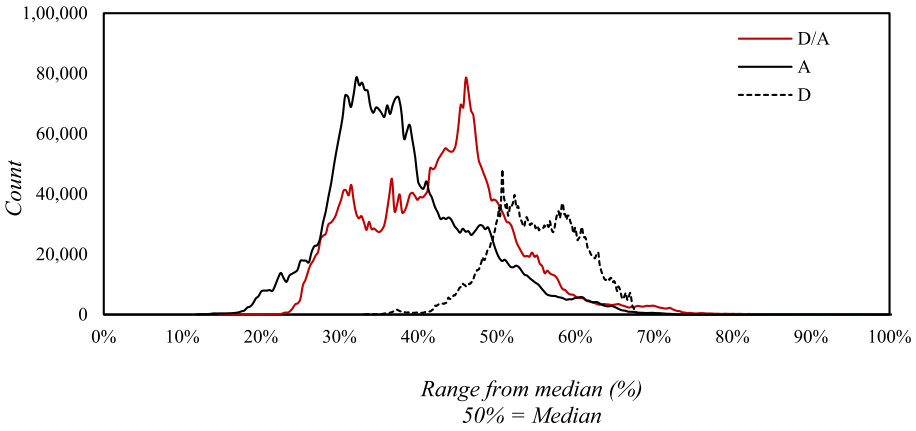

Fig. 20. Histograms of the topographical dataset distribution for scale-dependent parameter *D*, *A*, and D/A.

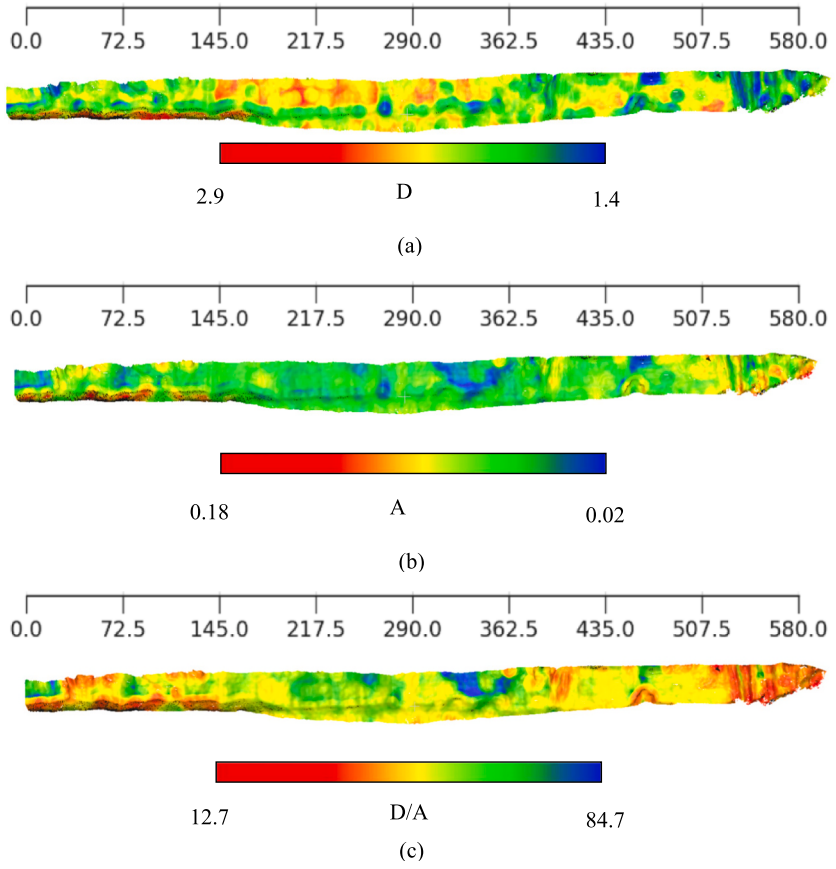

Fig. 21. Topographical model of the analysed pit wall with color scale for scale-dependent parameters (a) D, (b) A, and (c) D/A. Scale units are in meters (m). The recursive analysis was conducted with $r_w = 5$ m.

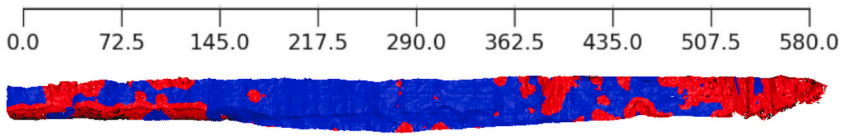

Fig. 22. Topographical model of the pit wall with a binary color scale using a threshold of $D/A = 34$.

situation, the sub-sections are characterized by cumulative fractions beyond a certain threshold as opposed to explicit zoning. The open-pit case study provided insightful information on the failure mechanism associated with the studied geometry, showcasing apparent pronounced shearing along one of the two structural planes.

The spatial variability associated with topographical conditions presents another insightful perspective towards objective geo-mechanical, geological, and operational differentiation. As noted with

the advancing mine tunnel (Fig. 16), blasting damage is not uniform and the topographical characterization is best described by spatial distribution of roughness conditions.

Figure 23 plots cumulative fraction (%) of the total point cloud with respect to measured parameters D/A. The cumulative passing representation distinguishes objectively the spatial distribution with respect to scale-dependent parameters for distinct geomechanical features. Fig. 23 (a) plots the cumulative distribution for the advancing tunnel. The exposed rock presents rougher overall conditions captured by lower values of D/A. Fig. 23 (b) plots the different cumulative distribution curves for the different topographical units observed in Fig. 12. It can be seen that the North structural plane and broken material surface present similar topographical conditions, while the South plane characterized by superficial shearing presents lower overall roughness conditions. Fig. 23 (c) plots the cumulative distributions for the advancing mine tunnel. The three subsets of the advancing mine cycles are characterized by progressively diminishing overall roughness as the cycle gets closer to freshly blasted conditions. Fig. 23 (d) shows the distinct spatial distributions between weathered surfaces and natural blocky conditions.

The cumulative distribution representation shown in Fig. 23 can further enhance the objective clustering of the topographical dataset. For case studies where clustering is required, the greatest spread in cumulative passing (vertical axis) is desired in order to better differentiate topographical units. For example, the limestone quarry case study binary threshold (Fig. 22) was set at $D/A = 34$. It can be seen from Fig. 23 (d) that the vertical spread at $D/A = 34$ between the weathered and blocky subsets is very large, thus offering a very objective framework towards differentiation. This approach can also be leveraged as an operational criterion towards various performance conditions (e.g., improving surface roughness of an excavation by shifting the curves to the right). This approach also offers an objective means to differentiate mixed conditions which are often encountered in realistic geological settings (see for example Fig. 8).

It is also inferred that the recursive scale-dependent analysis presented in this research, coupled with the cumulative passing distribution plots approach (Fig. 23) can provide a quantifiable perspective towards classification systems and spatial distribution. Considering for example the limestone quarry case study, the geomechanical change induced by mechanical erosion may decrease a GSI-based rating (Hoek et al., 1995) by as much as 20 points. Referring to Fig. 23 (d) and imposing binary threshold of $D/A = 34$ as the largest cumulative spread, it becomes possible to assign a statistical distribution (% fraction) of the model

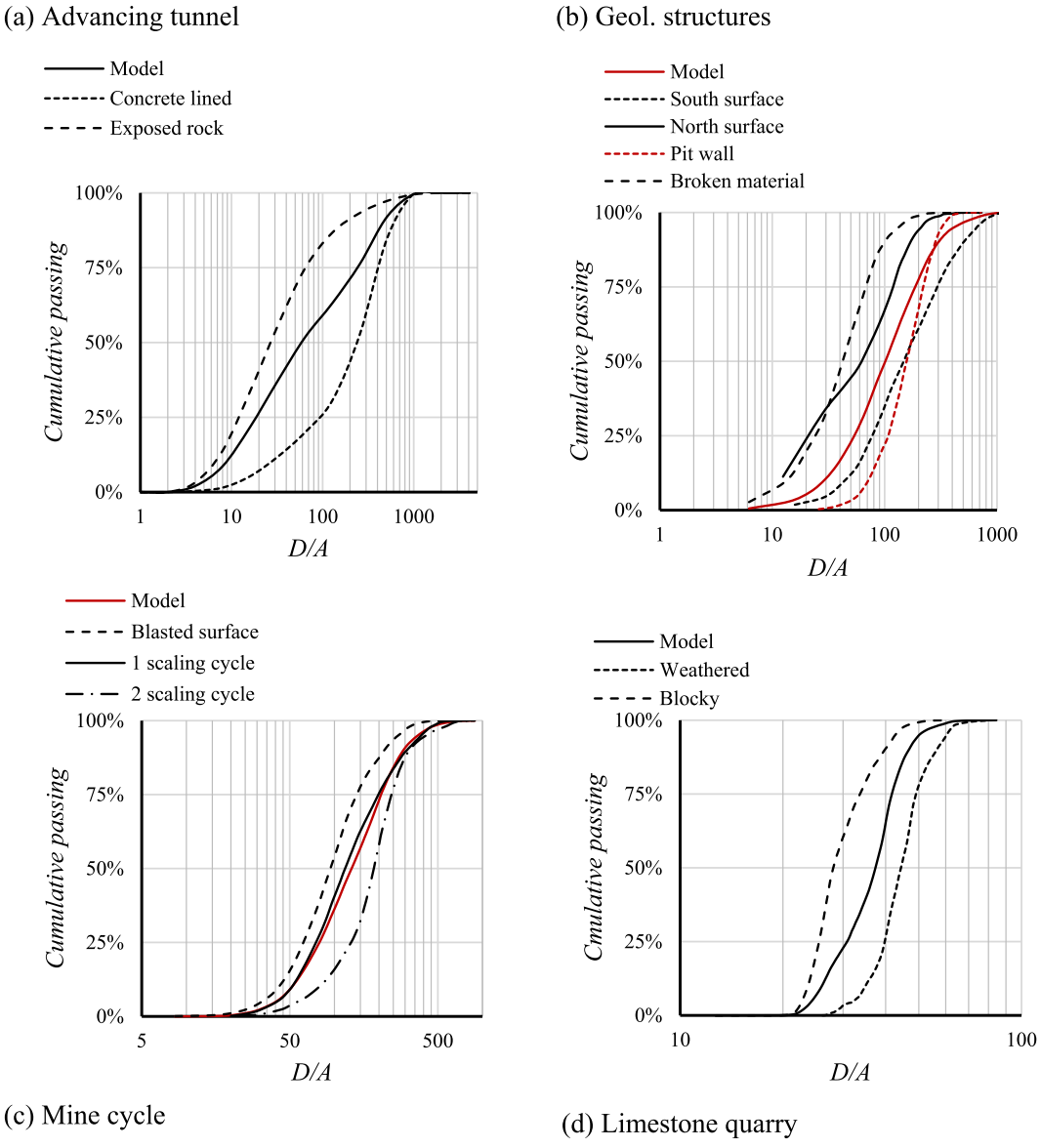

Fig. 23. Cumulative passing distribution for parameter D/A for the four case studies presented in this research.

associated with different classification values.

The work presented in this research implemented a number of predefined constraints pertaining to scales of measurements. Menezes et al. (2013) suggests using radius of measurement r greater than 5 to 10 times point spacing of the investigated point cloud. It is asserted from the different $\xi_r - r$ plots presented in this work (e.g., Fig. 5) that the exponent H (Eq. [1]) decreases when r is less than or equal to 3 times the point spacing, and can be used as a lower threshold for automated analysis.

The research presented in this work comprised procedural decisions that reflected special conditions specific to case studies considered. Point cloud density influences the range at which scale-dependent features can be observed. Fig. 24 shows the influence of varying density on multi-scale topographical analysis. Controlled subsampling of the point clouds was performed at 80 % and 20 % of the original number of points. Multi-scale topographical analysis was then conducted for each of the subsampled clouds. It is observed that scale-dependent trends vary with respect to density for small-scale conditions (i.e., $r < 0.1$). Such range is outside the scales considered for comparison analysis in the above work. Considering the corresponding average point spacing of the subsampled clouds, $\bar{s}$, it is inferred that density will influence scale-dependent trends for $r < 10\bar{s}$.

The selection of r_w is based on two main factors: the average point spacing and the intended application. The appropriate range for r_w is also determined from the range of radii used for the algorithm, where recursive linear regression is applied. Within this range, contrasting features remain distinguishable, ensuring effective analysis. Depending on the application and the extent of the scan, r_w is typically chosen between 10 times the average point spacing of the scan and 2.5 to 5 times the lower bound of the range used for the algorithm.

The scale of measurements implemented in this work captures relevant scales associated with mineralogical and physical (e.g., weathering) conditions. As noted by Shepard et al. (2001) for large landscapes, and Aubertin and Hutchinson (2022) for topographical datasets from underground mines, transition points are observed on the $\log(\xi) - \log(r)$ plots, reflecting a change in dominant scale-dependent features. For the first three case studies, a near-consistent range of approximate radii $0.1 \leq r \leq 1$ m is used to contrast topographical features. This range was also noted by Aubertin and Hutchinson (2022). The last case study involved a large-scale range of radii to contrast topographical features. Further automation of this process could implement iterative linear-regression to determine the best range of radii for specific case studies. It is emphasized however, that a sufficiently adequate range of contrasting radii can be determined from select subsamples following the rationale implemented in the different case studies (e.g., Fig. 19).

scale-dependent topographical characterization and differentiation has been used in the past to differentiate large-scale topographical features for extra-terrestrial bodies (Shepard et al., 2001), evaluate the performance of various rock excavation methods and processes (Aubertin et al., 2019; Aubertin and Hutchinson, 2022), and derive geomechanical parameters for rock interfaces (Grasselli, 2001). The present research expands from these niche applications to develop a systematic and objective classification and characterization method which can capture complex and mixed geomechanical and topographical conditions. It presents substantial potential for automation and integration to open-source software (e.g., CloudCompare).

The datasets investigated in this work captured a broad, albeit not exhaustive, spectrum of geomechanical settings corresponding to different geological conditions, weathering conditions, support systems, and excavation methods. The selection aimed to demonstrate the diverse applications of the method, and the fundamental objective nature of feature differentiation from topographical analysis. It is asserted based on the investigation carried out and the complex and diverse settings investigated, that the developed methodology has the potential to be replicated broadly to other geomechanical and operational settings not necessarily captured here.

Variable density and computational time represent additional limitations that may impede efficient and systematic implementation of the proposed method. As noted, point cloud density influences the window size r_w and the reliable range of radii where scale-dependent trends can be measured. The datasets presented in this work featured fairly homogeneous density, and advantageous point spacing, as demonstrated in Fig. 24. The figure also suggests that a lower density could have been used, and it is asserted that variable cloud density could be alleviated by

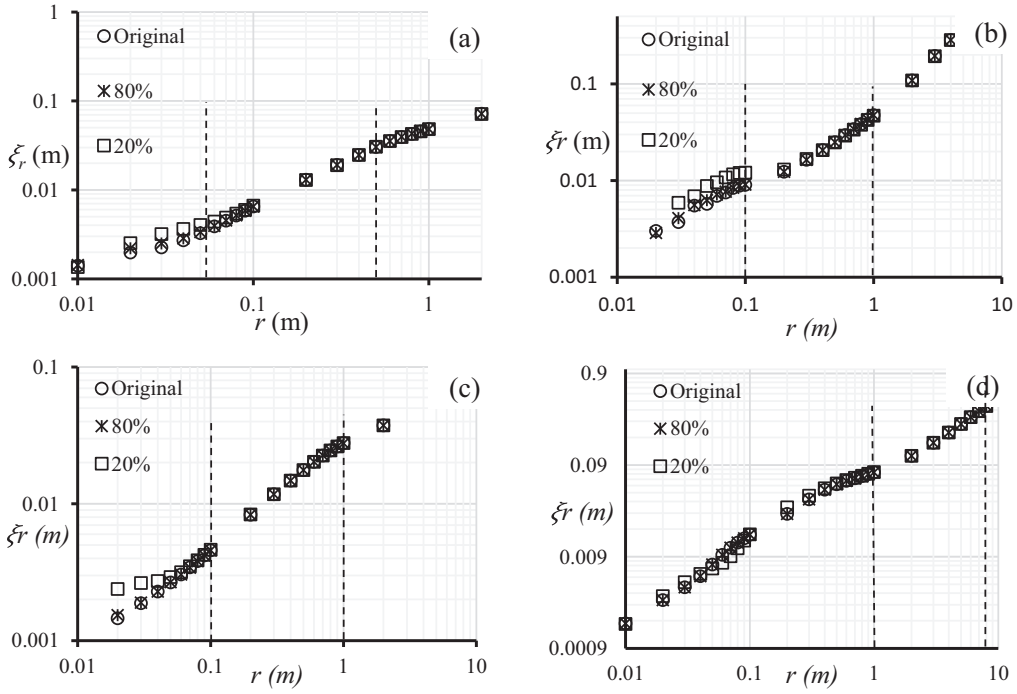

Fig. 24. Influence of variations in density on scale-dependent topographical analysis for (a) Advancing tunnel, (b) Graphite mine, (c) Pugwash mine drift, and (d) Limestone quarry.

controlled subsampling to homogenize point spacing without impacting the results. Computational times for $r > 1m$ can become prohibitive for larger datasets due to the recursive analysis framework. While not critical in the present study, this aspect could be alleviated by implementing octree-based (or similar) division schemes, and leveraging multi-core computing engines to reduce computational time.

6. Conclusion

This study introduces an automated algorithm for roughness-based geological and geomechanical differentiation from 3D point clouds, leveraging a scale-dependent approach to ensure robustness across varying geological conditions. Unlike traditional methods, which often rely on subjective or site-specific criteria, this approach provides a quantitative and adaptable framework for analyzing rock surfaces.

By employing a systematic, scale-dependent recursive analysis of roughness parameters derived from *3D* point cloud data, the research provides a robust framework for quantifying and classifying topographical features. The recursive method improves both accuracy and computational efficiency compared to traditional techniques. By capturing surface features at multiple scales, the method provides finer control over the analysis and reduces computational time, making it more efficient for large-scale applications in engineering geology. The recursive algorithm offers an objective methodology to identify and distinguish geological and geomechanical units across a wide range of operational settings. This helps reduce the human biases and errors that could arise from subjective interpretations, leading to more accurate assessments of the site's conditions.

The case studies presented in this research demonstrated the variability and spatial distribution of topographical features in natural and excavated rock outcrops, emphasizing how roughness parameters are affected by scale and measurement methods. These scale-dependent trends reveal the relationship between topography and geomechanical conditions and highlight their value in improving differentiation schemes towards engineering designs.

For all the case studies, the recursive automated analysis was conducted using measurement radii ranging from approximately 10 to 100 times the average point spacing of each scan. For the first three case studies, this corresponded to a range of approximately 0.1 m to 1 m, depending on the specific case and point cloud density, while for the last case study, the range was selected between 1 m and 7 m due to the scan extent and the dimensions of contrasting features. In all cases, the smallest radius used for r_w was 10 times the average point spacing of the scan. However, for some cases, depending on the specific application, it was chosen to be 2.5 to 5 times the lower bound of the radii used for the algorithm. The exponent H varied across different geomechanical components. For example, shotcrete and highly sheared surfaces exhibited lower roughness and higher H values, whereas freshly blasted or exposed rock surfaces on tunnel walls showed greater roughness and lower H values. These variations correspond to fractal dimensions, with $D = 3 - H$. The transition in these values reflects clear differences in surface morphology across operational and geological contexts. Furthermore, ratios such as D/A were used as indicators for clustering and binary thresholding, with effective thresholds (e.g., $D/A = 34$) identified for differentiating weathered from intact zones. The influence of point cloud density was evaluated through controlled subsampling, which showed a negligible effect on the analysis results within the selected scale range, provided that $r \geq 10\overline{s}$. These findings establish a clear link between spatial resolution, scale selection, and geomechanical interpretation, reinforcing the robustness of the proposed methodology.

The cumulative passing distribution plots, as exemplified in Fig. 23, further enhance the differentiation framework by providing a quantifiable basis for spatial and operational clustering. This approach offers practical implications towards site-specific considerations such as blasting performance optimization. Moreover, the findings underscore the potential of this methodology to complement and refine existing classification systems, such as GSI-based ratings, by incorporating statistically robust topographical criteria.

In conclusion, the integration of scale-dependent roughness analysis and automated clustering represents a significant advancement in the objective characterization of rock outcrops. The proposed framework holds promise for enhancing geomechanical differentiation and advancing geoengineering practices in mining, tunneling, and construction applications. Beyond geoengineering fields, this methodology has the potential to benefit several other domains, including planetary geology, environmental monitoring, and geohazard assessment. The methodology presented in the research offers an objective characterization for varying topographical features which can be applied to differentiate extraterrestrial landscapes, and distinguish the level of superficial deterioration induced by chemical agents. Further research should also be carried out to leverage this approach to detect geohazard failure precursors which could reveal changes, along certain scales, in superficial roughness conditions (e.g., surface erosion prior to landslides yielding localized changes in superficial roughness).

CRediT authorship contribution statement

Niloufarsadat Sadeghi: Writing – original draft, Visualization, Methodology, Investigation, Formal analysis, Data curation, Conceptualization. **Jonathan D. Aubertin:** Writing – review & editing, Validation, Supervision, Resources, Project administration, Investigation, Funding acquisition, Conceptualization.

Funding

This work was supported by the National Sciences and Engineering Research Council of Canada through the Discovery Grant program (RGPIN-2022-03893), and by national research organization MITACS (Project IT39336).

Declaration of competing interest

The authors declare the following financial interests/personal relationships which may be considered as potential competing interests:

Niloufarsadat Sadeghi reports financial support was provided by National Sciences and Engineering Research Council of Canada. Niloufarsadat Sadeghi reports financial support was provided by Mitacs Inc. If there are other authors, they declare that they have no known competing financial interests or personal relationships that could have appeared to influence the work reported in this paper.

Data availability

Data will be made available on request.

References

Aubertin, J.D., Hutchinson, D.J., 2022. Scale-dependent rock surface characterization using LiDAR surveys. Eng. Geol. 301, 106614. https://doi.org/10.1016/j.enggeo.2022.106614. Available at:

Aubertin, J.D., Hutchinson, D.J., Diederichs, M.S., 2019. Application of LiDAR technology for the assessment of mechanical scaling conditions in underground mines and tunnels. In: Proceedings of GeoSt-John's 2019. St. John's, Newfoundland and Labrador, Canada. Canadian Geotechnical Society, St. John's.

Azarafza, M., et al., 2019. Development of a 2D and 3D computational algorithm for discontinuity structural geometry identification by artificial intelligence based on image processing techniques. Bull. Eng. Geol. Environ. 78 (5), 3371–3383. Available at: https://doi.org/10.1007/s10064-018-1298-2.

Azarafza, M., Koçkar, M.K., Faramarzi, L., 2021. Spacing and block volume estimation in discontinuous rock masses using image processing technique: a case study. Environ. Earth Sci. 80 (14). https://doi.org/10.1007/s12665-021-09768-3. Available at:

Bagde, M.N., et al., 2002. Rock mass characterization by fractal dimension. Eng. Geol. 63 (1), 141–155. Available at: https://doi.org/10.1016/S0013-7952(01)00078-3.

Ban, L., Du, W., Qi, C., 2020. A modified roughness index based on the root mean square of the first derivative and its relationship with peak shear strength of rock joints.

Eng. Geol. 279, 105898. Available at: https://doi.org/10.1016/j.enggeo.2020.105898.
Bao, H., et al., 2020. Geometrical heterogeneity of the joint roughness coefficient revealed by 3D laser scanning. Eng. Geol. 265, 105415. Available at: https://doi.org/10.1016/j.enggeo.2019.105415.
Barton, N., 1973. Review of a new shear-strength criterion for rock joints. Eng. Geol. 7 (4), 287–332. Available at: https://doi.org/10.1016/0013-7952(73)90013-6.
Barton, N., Lien, R., Lunde, J., 1974. Engineering classification of rock masses for the design of tunnel support. Rock Mech. Felsmechanik Mécanique Roches 6 (4), 189–236. Available at: https://doi.org/10.1007/BF01239496.
Barton, N., Wang, C., Yong, R., 2023. Advances in joint roughness coefficient (JRC) and its engineering applications. J. Rock Mech. Geotech. Eng. 15 (12), 3352–3379. Available at: https://doi.org/10.1016/j.jrmge.2023.02.002.
Berti, M., Corsini, A., Daehne, A., 2013. Comparative analysis of surface roughness algorithms for the identification of active landslides. Geomorphology 182, 1–18. Available at: https://doi.org/10.1016/j.geomorph.2012.10.022.
Bieniawski, Z.T., 1989. Engineering Rock Mass Classifications: A Complete Manual for Engineers and Geologists in Mining, Civil, and Petroleum Engineering. John Wiley & Sons, New York, NY.
Chae, B.G., et al., 2004. Roughness measurement of rock discontinuities using a confocal laser scanning microscope and the Fourier spectral analysis. Eng. Geol. 72 (3), 181–199. Available at: https://doi.org/10.1016/j.enggeo.2003.08.002.
Fardin, N., 2008. Influence of structural non-stationarity of surface roughness on morphological characterization and mechanical deformation of rock joints. Rock Mech. Rock. Eng. 41 (2), 267–297. Available at: https://doi.org/10.1007/s00603-007-0144-9.
Fardin, N., Feng, Q., Stephansson, O., 2004. Application of a new in situ 3D laser scanner to study the scale effect on the rock joint surface roughness. Int. J. Rock Mech. Min. Sci. 41 (2), 329–335. Available at: https://doi.org/10.1016/S1365-1609(03)00111-4.
FARO Technologies, 2021. FARO Laser Scanner Focus User Manual. Lake Mary, Florida.
Ge, Y., et al., 2022. A low-cost approach for the estimation of rock joint roughness using photogrammetry. Eng. Geol. 305, 106726. Available at: https://doi.org/10.1016/j.enggeo.2022.106726.
Glenn, N.F., et al., 2006. Analysis of LiDAR-derived topographic information for characterizing and differentiating landslide morphology and activity. Geomorphology 73 (1–2), 131–148. Available at: https://doi.org/10.1016/j.geomorph.2005.07.006.
Grasselli, G., 2001. Shear Strength of Rock Joints Based on Quantified Surface Description (Doctoral Dissertation). ETH Zurich Research Collection.
Guo, Y., et al., 2022. Quantitative Characterization Method for Rock Surface Roughness with Different Scale fluctuation. KSCE J. Civ. Eng. 26 (4), 1695–1711. Available at: https://doi.org/10.1007/s12205-022-1228-5.
Hoek, E., 2007. Practical Rock Engineering. Evert Hoek Consulting Engineer Inc, North Vancouver, BC.
Hoek, E., Marinos, P., 2007. A brief history of the development of the Hoek-Brown failure criterion. Soils Rocks 2 (2), 2–13.
Hoek, E., Kaiser, P.K., Bawden, W.F., 1995. Support of Underground Excavations in Hard Rock. Balkema, Rotterdam. https://doi.org/10.1201/b16978. Available at:
Hyslip, J.P., Vallejo, L.E., 1997. Fractal analysis of the roughness and size distribution of granular materials. Eng. Geol. 48 (3), 231–244. Available at: https://doi.org/10.1016/S0013-7952(97)00046-X.
ISRM, 1978. Suggested methods for determining tensile strength of rock materials. Int. J. Rock Mech. Min. Sci. Geomech. Abstr. 15 (3), 99–103. Available at: https://doi.org/10.1016/0148-9062(78)90003-7.
Kolay, E., Kayabali, K., 2006. Investigation of the effect of aggregate shape and surface roughness on the slake durability index using the fractal dimension approach. Eng. Geol. 86 (4), 271–284. Available at: https://doi.org/10.1016/j.enggeo.2006.05.007.
Lai, P., Samson, C., Bose, P., 2014. Surface roughness of rock faces through the curvature of triangulated meshes. Comput. Geosci. 70, 229–237. Available at: https://doi.org/10.1016/j.cageo.2014.05.010.
Lê, H.K., et al., 2018. Spatial characteristics of rock joint profile roughness and mechanical behavior of a randomly generated rock joint. Eng. Geol. 245, 97–105. Available at: https://doi.org/10.1016/j.enggeo.2018.06.017.
Lee, Y.-H., et al., 1990. The fractal dimension as a measure of the roughness of rock discontinuity profiles. Int. J. Rock Mech. Min. Sci. Geomech. Abstr. 27 (6), 453–464. Available at: https://doi.org/10.1016/0148-9062(90)90998-H.
Li, B., et al., 2023. Approach to characterize rock fracture surface: insight from roughness and fractal dimension. Eng. Geol. 325, 107302. Available at: https://doi.org/10.1016/j.enggeo.2023.107302.
Li, Y., Huang, R., 2015. Relationship between joint roughness coefficient and fractal dimension of rock fracture surfaces. Int. J. Rock Mech. Min. Sci. 75, 15–22. Available at: https://doi.org/10.1016/j.ijrmms.2015.01.007.
Liu, X., et al., 2022. Reconstruction of rough rock joints: 2D profiles and 3D surfaces. Int. J. Rock Mech. Min. Sci. 156, 105113. Available at: https://doi.org/10.1016/j.ijrmms.2022.105113.
Liu, X.G., et al., 2017. Estimation of the joint roughness coefficient of rock joints by consideration of two-order asperity and its application in double-joint shear tests. Eng. Geol. 220, 243–255. Available at: https://doi.org/10.1016/j.enggeo.2017.02.012.
Magsipoc, E., Zhao, Q., Grasselli, G., 2020. 2D and 3D roughness characterization. Rock Mech. Rock. Eng. 53 (3), 1495–1519. Available at: https://doi.org/10.1007/s00603-019-01977-4.
Mandelbrot, B., 1967. How long is the coast of Britain? Statistical self-similarity and fractional dimension. Science 156 (3775), 636–638. Available at: https://doi.org/10.1126/science.156.3775.636.
McKean, J., Roering, J., 2004. Objective landslide detection and surface morphology mapping using high-resolution airborne laser altimetry. In: Geomorphology. Elsevier, pp. 331–351. Available at: https://doi.org/10.1016/S0169-555X(03)00164-8.
Menezes, P.L., Kailas, S.V., Lovell, M.R., 2013. Fundamentals of Engineering Surfaces. In: Menezes, P.L., et al. (Eds.), Tribology for Scientists and Engineers: From Basics to Advanced Concepts. Springer, New York, NY, pp. 3–41. Available at https://doi.org/10.1007/978-1-4614-1945-7_1.
Niknezhad, M., et al., 2024. Topographical investigation of rock slope failure modes in a surface pit repurposed for storage of snow debris. In: Proceedings of Geomontreal. Montreal, Quebec, Canada. Canadian Geotechnical Society, Montreal.
Poropat, G.V., 2008. Remote characterisation of surface roughness of rock discontinuities. In: Proceedings of the First Southern Hemisphere International Rock Mechanics Symposium (SHIRMS 2008), Perth, Western Australia. Australian Centre for Geomechanics, Perth, Western Australia. https://doi.org/10.36487/ACG_repo/808_123. Available at:
Python Software Foundation, 2023. Python language reference (3.11.7). Python Software Foundation. Available at: https://docs.python.org/3.11/reference/index.html (Accessed: 7 January 2025).
Sadeghi, N., Aubertin, J.D., Deminiat, A., 2023. Geological and geomechanical differentiation of rock interfaces based on recursive multi-scale analysis with topographical data sets. In: Proceedings of GeoSaskatoon2023. Saskatoon, Saskatchewan, Canada. Canadian Geotechnical Society, Saskatoon.
Shepard, M.K., et al., 2001. The roughness of natural terrain: a planetary and remote sensing perspective. J. Geophys. Res. E: Planets 106 (E12), 32777–32795. Available at: https://doi.org/10.1029/2000JE001429.
Singh, H.K., Basu, A., 2018. Evaluation of existing criteria in estimating shear strength of natural rock discontinuities. Eng. Geol. 232, 171–181. Available at: https://doi.org/10.1016/j.enggeo.2017.11.023.
Stewart, J., 2003. Calculus: Early Transcendentals, 6th edn. Brooks/Cole, Belmont, California.
Stigsson, M., Mas Ivars, D., 2019. A novel conceptual approach to objectively determine JRC using fractal dimension and asperity distribution of mapped fracture traces. Rock Mech. Rock. Eng. 52 (4), 1041–1054. Available at: https://doi.org/10.1007/s00603-018-1651-6.
Tatone, B.S.A., Grasselli, G., 2010. A new 2D discontinuity roughness parameter and its correlation with JRC. Int. J. Rock Mech. Min. Sci. 47 (8), 1391–1400. Available at: https://doi.org/10.1016/j.ijrmms.2010.06.006.
Tatone, B.S.A., Grasselli, G., 2013. An investigation of discontinuity roughness scale dependency using high-resolution surface measurements. Rock Mech. Rock. Eng. 46 (4), 657–681. Available at: https://doi.org/10.1007/s00603-012-0294-2.
Zheng, B., Qi, S., 2016. A new index to describe joint roughness coefficient (JRC) under cyclic shear. Eng. Geol. 212, 72–85. Available at: https://doi.org/10.1016/j.enggeo.2016.07.017.